Arab J Geosci
DOI 10.1007/s12517-014-1562-0

ORIGINAL PAPER

Mapping of the late Neoproterozoic Basement rocks and detection of the gold-bearing alteration zones at Abu Marawat-Semna area, Eastern Desert, Egypt using remote sensing data

S. M. Hassan · T. M. Ramadan

Received: 7 May 2014 / Accepted: 14 July 2014

Abstract Intensive investigation of the basement rock units of Abu Marawat-Semna area in the northern part of Central Eastern Desert of Egypt and their gold-bearing alteration zones using remote sensing techniques is accomplished. The study area consists of a Pan-African tectono-stratigraphic sequence, where allochthonous sheets and slices of ophiolitic serpentinite-talc-carbonate components were thrusted onto an island-arc metavolcanics. These rocks were later intruded by gabbro-diorite and biotite granite and invaded by a network of quartz veins, which are locally charged with gold. The visible near-infrared (VNIR) and short-wave infrared (SWIR) reflectance data of Advanced Spaceborne Thermal Emission and Reflection Radiometer (ASTER) imagery and Landsat 8 data were employed in the detailed geological mapping and detection of mineralized alteration zones. The results show that Landsat 8 band ratio image (b6/b2, b6/b7, and b6/b5×b4/b5) distinguishes the lithological units. Two different types of alteration zones (1 and 2) have been recognized in the study area using ASTER spectral characteristic analysis (SCA), band ratios, principle component analysis (PCA), Minimum Noise Fraction (MNF) techniques and ascertained by field verification, XRD, and XRF investigations. Type 1 (carbonate are the main phases) is mainly confined to the ophiolitic serpentinite-talc-carbonate rocks, whereas type 2 (quartz, sericite, and kaolinite-rich alteration zone are the main phases) is located within island-arc metavolcanics. The geochemical studies recorded anomalous contents of Cr and Ni in the alteration zone type 1 while Cr reaches 1,549 ppm and Ni abundance attains about 1,052 ppm. The investigated alteration zone type 2 in the metavolcanics recorded the presence of high anomalous contents of gold (up to 36 ppm), silver (up to 200 ppm), zinc (up to 3,992 ppm), and copper (up to 83,720 ppm). The geochemical study indicates that the detected alteration zones in the metavolcanics and the ophiolitic ultramafic rocks are promising and need more detailed exploration for Au and Ag mineralization. The study proves the potentiality of the alteration zones in and around the ophiolitic serpentinite-talc-carbonate rocks and their intimately associated island-arc metavolcanics. The image processing of the remote sensing data as proposed in the present study proves its high capability in detecting the mineralized alteration zones in other tectonically and geologically similar arid regions in the Arabian-Nubian Shield (ANS) and worldwide.

Keywords Abu Marawat-Semna · Remote sensing · ASTER · Landsat 8 · Arabian-Nubian Shield · Mineralized alteration zones

Introduction

With the development of remote sensing technology that provides detailed information on mineralogy of different rock types on the Earth's surface (e.g., Zhang et al. 2007), many image processing methodologies have been developed that attempt to map boundaries of rock bodies, weathered rock zones, and hydrothermally altered rock zones, especially in arid regions where vegetation cover is minimal (e.g., Sultan and Arvidson 1986; Loughlin 1991; Rokos et al. 2000; Abdelsalam and Stern 2000; Ramadan et al. 2001; Kusky and Ramadan 2002; Ferrier et al. 2002; Sadek 2004, 2005; Liu et al. 2007; Zhang et al. 2007; Gabr et al. 2010; Ali-Bik et al. 2012; Zoheir and Emam 2012a, b; Abou Elmagd et al. 2013). The multispectral remote

S. M. Hassan (✉) · T. M. Ramadan
National Authority for Remote Sensing and Space Sciences ?(NARSS), Cairo, Egypt
e-mail: Safaa.hassan@narss.sci.eg

S. M. Hassan
e-mail: safaamh2002@yahoo.com

Published online: 23 July 2014

sensing techniques with different spatial and spectral resolutions have played a crucial and economically effective role in detecting and tracing the potential alteration zones around gold-bearing quartz lodes in particular and other ores in general.

Strictly speaking, the spectral discrimination of potential areas of gold mineralization (e.g., hydrothermal alteration zones and iron gossans) is a well-established application of remote sensing (e.g., Abdelsalam and Stern 2000; Zhang et al. 2007; Rajendran et al. 2013). Many authors have studied the spectral characteristics related to this type of target using the data set obtained from different satellite sources such as Landsat TM, Landsat Enhanced Thematic Mapper Plus (ETM+), and the Advanced Spaceborne Thermal Emission and Reflection Radiometer (ASTER). A range of image processing techniques such as band rationing, Minimum Noise Fraction (MNF), principal component analysis (PCA) and Spectral Characteristics analysis (SCA) have been applied by several authors (e.g., Loughlin 1991; Rokos et al. 2000; Ferrier et al. 2002; Gabr et al. 2010; Abrams and Hook 1995; Sabins 1997, 1999; Cudahy et al. 2000; Rowan and Mars 2003; Rowan et al. 2003; Ninomiya 2003; Mars and Rowan 2006; Gad and Kusky 2007; Amer et al. 2010, 2012; Sadek and Hassan 2012).

In the Eastern Desert of Egypt, more than 95 gold occurrences are known and have been exploited as early as the predynastic times and up to the fifth century, when these mines were abandoned (Hume 1937). However, with the technological development of gold exploration techniques and based on pure economic perspectives, commercial interest

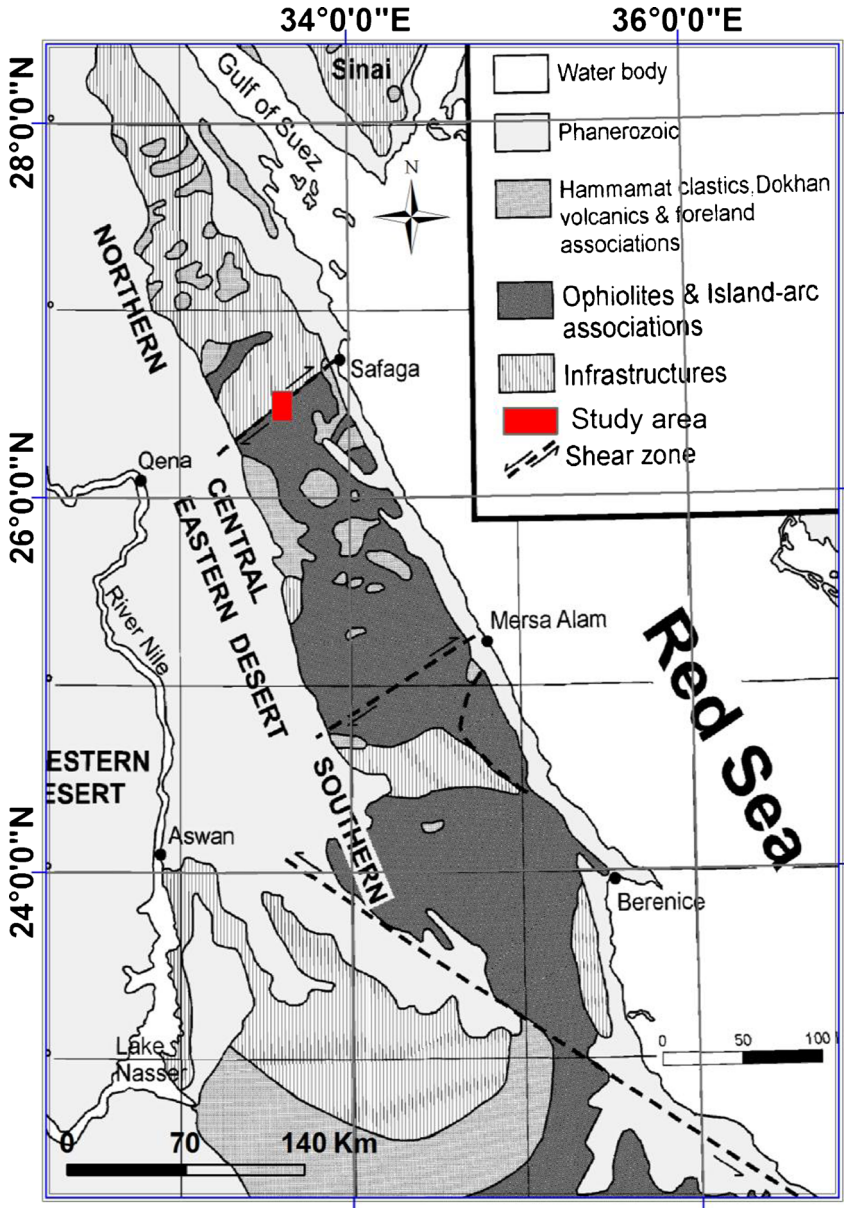

Fig. 1 **a** Regional geological map (after El Gaby et al. 1988) shows the location map of the study area

has been rekindled to explore and reevaluate searching for old Egyptian gold mines with special emphasis on the alteration zones of significant gold-bearing quartz lodes (e.g., Hume 1937; Sabet et al. 1976; Sabet and Bordonosov 1999; David 1988; El Gaby et al. 1988; Botros 1991, 1993b, 1995a, 1995b, 2002a, 2002b, 2004; Zoheir et al. 2008).

The present study presents the results of remote sensing techniques used for mapping of the Late Neoproterozoic basement rocks of Abu Marawat-Semna area, Eastern Desert of Egypt, with special emphasis on detecting the presence of gold-bearing alteration zones in the area. Several remote sensing data processing techniques were applied in conjunction with field data to discriminate the different rock units of the area. The visible near-infrared (VNIR) and short-wave infrared (SWIR) reflectance data of ASTER imagery and Landsat 8 were evaluated as tools for discriminating and mapping lithological units and gold-bearing alteration zones. To validate the applied remote sensing techniques, mineralogical and geochemical investigations were carried out to characterize the altered phases in hydrothermally altered zones. A new detailed map of the study area has been accomplished using the spectral signature of the exposed rock units and related minerals.

Regional geology

Abu Marawat-Semna area is located south of the Safaga–Qena Road, in the Eastern Desert of Egypt between latitudes 26° 25′ and 26° 32′ N and longitudes 33° 33′ and 33° 40′ E (Fig. 1), covering an area of approximately 190 km^2. The basement geology of Abu Marawat-Semna consists of lithologic units which were formed during the Neoproterozoic Pan-African orogeny (Stern 1994; Kusky et al. 2003; Kröner 1984; Kröner et al. 2003). The rocks evolved in an arc-back-arc basin environment (Dardir and Al-Wakeel 1998; El-Shazly and El-Sayed 2000) and it is mostly represented by the Abu Marawat arc, volcano-sedimentary sequence (Botros 1991, 2002a, 2004; Fowler et al. 2006) that was regionally metamorphosed to green schist facies. Several authors (El-Mezayen, et al. 1995; Gabr et al. 2010; Zoheir et al., 2008) studied the geologic and tectonic setting of some parts of the study area and arranged the rock units from oldest to youngest as follows: highly sheared serpentinites and talc-carbonate rocks, metavolcanics, gabbro-diorite, Hammamat sediments, Dokhan volcanics, and Younger Granites.

The serpentinites and talc-carbonates are highly sheared with foliations striking N-S and dipping about 70° to the west (El-Mezayen et al. 1995). It is now agreed upon that these and other major serpentinite ranges in the Eastern Desert of Egypt represent allochthonous ophiolitic components that were thrusted onto the nearby island-arc metavolcanics (El Gaby et al. 1990; Hassan and Hashad 1990). The metavolcanics represent the predominant rock unit in the study area, accounting for about 55 % of the area, and commonly containing interlayers of folded Banded Iron Formation (BIF) at Gabal Abu Marawat. These rocks have been metamorphosed under the conditions of greenschist facies and intruded by alkaline quartz diorite plutons (Farahat et al. 2007; Mohamed and

Table 1 Characteristics of ASTER and Landsat 8 remote sensing data

Subsystems	ASTER Bands	ASTER Spectral range (μm)	ASTER Spatial Resolution (m)	Landsat 8 Spectral bands (μm)	Landsat 8 spatial resolution (m)
	Band 1	0.52–0.60		Band 1: 0.433–0.453	30
VNIR	Band 2	0.63–0.69	15	Band 2: 0.450–0.515	30
	Band 3N	0.78–0.86		Band 3: 0.525–0.600	30
	Band 4B	1.60–1.70		Band 4: 0.630–0.680	30
				Band 5: 0.845–0.885	30
				Band 8: 0.500–0.680	15
				Band 9: 1.360–1.390	30
	Band 5	2.145–2.185			
SWIR	Band 6	2.185–2.225		Band 6:1.560–1.660	30
	Band 7	2.235–2.285		Band 7:2.100–2.300	30
	Band 8	2.295–2.365	30		
	Band 9	2.360–2.430			
	Band 10	8.125–8.475		Band 10: 10.6-11.2	100
TIR	Band 11	8.475–8.825		Band 11: 11.5-12.5	100
	Band 12	8.925–9.275	90		
	Band 13	10.25–10.95			
	Band 14	10.95–11.65			

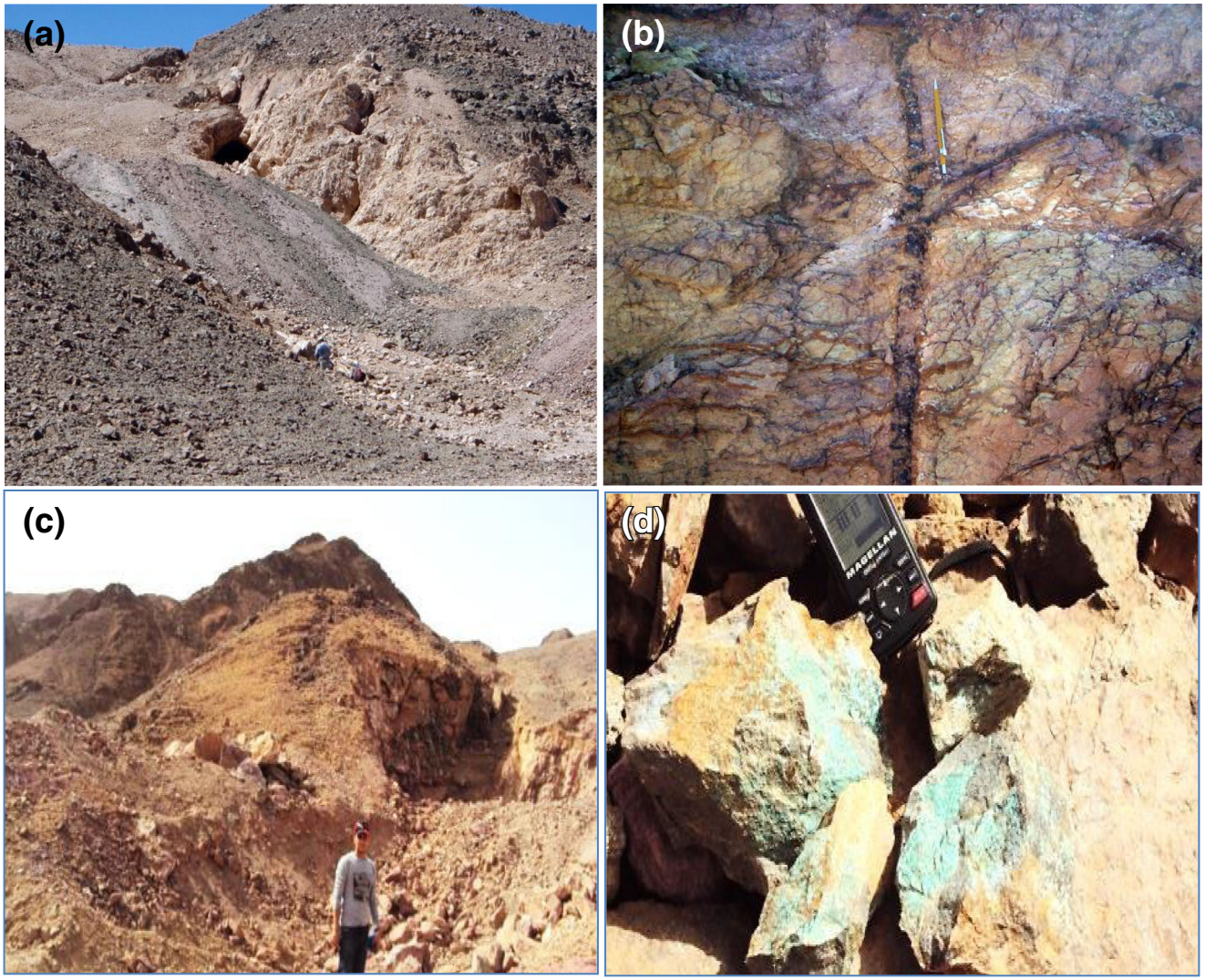

Fig. 2 **a** Alteration zone type 1 in serpentinite-talc-carbonate rocks, Semna area. Photo looking west. **b** Furriginated quartz veins dissecting metavolcanics in the alteration zone type 2, Abu Marawat area. Photo looking south. **c** Highly silicified and kaolintized alteration zone type 2 in metavolcanics, Abu Marawat area. Photo looking south. **d** Metavolcanics in alteration zone type 2 stained with malachite, Abu Marawat area. Photo looking southeast

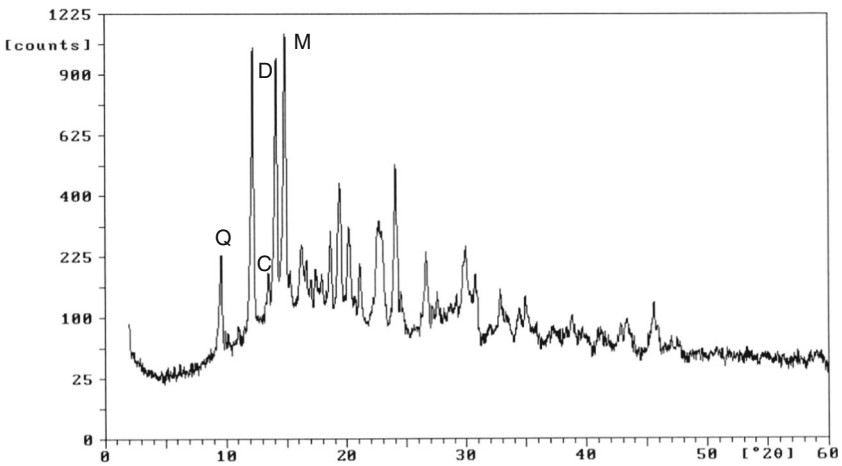

Fig. 3 XRD analysis for alteration zone type (1), Semna area. (Symbols *M*, *D*, *C*, and *Q* refer to magnesite, dolomite calcite and quartz, respectively)

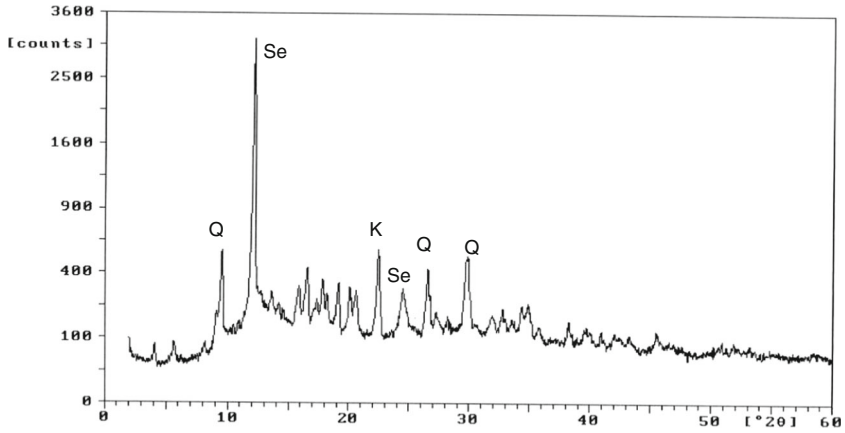

Fig. 4 XRD analysis for alteration zone type (2), Semna area. (Symbols *Q*, *Se*, and *K* refer to quartz, sericite, and kaolinite, respectively)

El-Sayed 2007). The folded BIF capping Gabal Abu Marawat metavolcanics is located at the northeastern part of the study area and has fold axes trending NNW (Botros 2004; Fowler et al. 2006). According to Basta et al. (2000), the BIF is of volcanogenic origin and could be related to the nearby metavolcanics. The BIF layers are made up of haematite- and magnetite-rich layers alternating with silica-rich bands as thin horizons within the volcano-sedimentary succession. Gold concentrations in the BIF layers are up to 2.15 ppm (Botros 1991). Botros (2004) related the gold mineralization to the interaction between hot brine fluids and seawater. The brines were capable of leaching iron, silica, gold, and other elements from the volcanic rocks that precipitated the BIF as chemical sediments when mixed with seawater.

The gabbro-diorite rocks of the Semna area have been studied by many authors (Bishara and Habib 1973; Aly et al. 1991). Along the contacts with the younger granites Semna area, the gabbro is injected by quartz veins and exhibits various degrees of alterations, which are most common and more extensive in the Semna gold mine area (Zoheir et al. 2008). According to El-Mezayen et al. (1995) and Zoheir et al. (2008), the mineralized quartz veins of both Abu Marawat and Semna are coeval in origin and can be attributed to the Dokhan volcanics. At Abu Marawat, only gold-bearing quartz veins were been exploited by the ancient miners, with open pit mining reaching a depth of about 40 m. Exclusively, all the old gold workings of the area are located within the metavolcanics along a N-S striking shear zone that hosts both auriferous quartz veins and iron gossans and extends southward as far as Semna. The N-S and NNW-SSE auriferous quartz veins represent an early hydrothermal event in the area (El-Mezayen et al. 1995).

Table 2 Major oxides (wt. %) of the mineralized zones

	Alteration zone 2		Alteration zone 1	
Oxides	S8	S10	S19	S16
SiO_2	74.05	75.56	12.2	16.5
TiO_2	0.27	0.21	0.02	0.02
AL_2O_3	16.06	14.17	0.46	0.16
Fe_2O_3	2.41	1.73	5.2	7.8
MnO_2	0	0	0.54	0.43
MgO	0.38	0.37	18.1	22.5
CaO	<0.01	<0.01	22.5	10.5
Na_2O	<0.01	<0.01	0.01	<0.01
K_2O	3.2	3.79	0.09	0.04
P_2O_5	0.02	0.06	0.01	0.01
CI	<0.01	<0.01	<0.01	<0.01
S	<0.01	<0.01	0.35	0.19
L.O.I.	3.24	4.1	40.3	41.54

Table 3 Trace elements contents (ppm) in the two mineralized alteration zones

	Alteration zone 2		alteration zone 1	
Trace elements	S8	S10	S19	S16
Ba	497.8	524.2	3.7	4.1
Co	5.9	5.3	44.3	70.4
Cr	32.5	29.2	892.7	1548.6
Nb	16.2	16	0.8	1
Ni	7.5	7	229.2	1051.8
Rb	86	87.5	0.3	0.3
V	55	34.7	18.7	21.3
Y	27.2	26.9	17.2	20.5
Cu	3.6	2.5	7.5	8.8
Zn	53	52.6	30.3	30
Zr	104.3	127.1	13.4	12.1
Sr	100.8	180.8	3.2	2.2
La	21.5	21.3	0.1	0.1
Ce	49	45.2	0.1	0.1
Pb	24.6	23.8	9.1	11.1

Material and methods

Remote sensing data

Landsat 8 (launched on February 11, 2013) measures different ranges of frequencies along the electromagnetic spectrum; it has 11 spectral bands (Table 1), covering the VNIR (bands 1–9), SWIR (bands 6 and 7), and the thermal infrared (TIR) (bands 10 and 11) reflectance data. Band 1 senses deep blues and violets, while bands 2, 3, and 4 are visible blue, green, and red, respectively. Band 5 measures the near infrared (NIR), while bands 6 and 7 cover different slices of the SWIR. Band 8 is the panchromatic band with a resolution of 15 m, and band 9 covers a very thin slice of wavelengths (only 1,370±10 nm). All of these characteristics make this satellite technically advanced and widen its capabilities for imaging and monitoring the following: (a) shallow water and fine particles like dust and smoke (band 1), (b) ecological systems (band 5), (c) wet and dry earth as well as rocks and soils (bands 6 and 7), these bands are very useful for geological mapping purposes.

ASTER was launched in December 1999 and has provided higher spectral resolution data facilitating mineral exploration (Di Tommaso and Rubinstein 2007). ASTER data consists of 14 data channels that cover ranges of visible, near-infrared (VNIR), SWIR, and thermal infrared (TIR) regions of the electromagnetic spectrum (Table 1). It covers an area of 60×60 km^2 and provides higher spatial and spectral resolutions than Landsat 7 data (Abrams and Hook 1995) while Landsat 8 has higher radiometric resolution (16 bit). The spatial resolution of VNIR, SWIR, and TIR is 15, 30, and 90 m, respectively (Table 1). The narrower band width of the ASTER SWIR region is more accurate in the spectral identification of rocks and minerals than Landsat or SPOT data (Crósta and Filho 2003).

ASTER measures visible reflected radiation in three VNIR spectral bands between 0.52 and 0.86 μm, with 15-m spatial resolution and infrared reflected radiation in six shortwave infrared spectral bands SWIR between 1.6 and 2.43 μm, with 30-m spatial resolution. In addition, ASTER records the data in band 3B (0.76–0.86 μm) with a backward looking VNIR telescope that enables the calculation of digital elevation model (DEM). Moreover, emitted radiation is measured at 90-m resolution in five bands (8.125–11.65 μm) in the thermal infrared wavelength region (TIR). The swath width is 60 km, but ASTER's pointing capability extends the total cross-track viewing capability to 232 km (Fujisada 1995a, b). Image analysis techniques such as PCA and band ratios are based on the spectral characteristics of surface types. Many authors have used different remote sensing techniques designated for target detection, including constrained energy minimization (CEM) (Chang and Heinz 2000; Settle 2002), PCA (Loughlin 1991; Rokos et al. 2000; Crósta and Filho 2003), band ratios (Sultan and Arvidson 1986; Rokos et al. 2000; Xu et al. 2004), or both band ratios and PCA combined (Zhang et al. 2007).

The applied image processing techniques

The image processing techniques were carried out on an ASTER level 1B image acquired on January 29, 2003. This scene is orthorectified using DEM using UTM projection and WGS-84 for ellipsoid. The ASTER scene covering the study area was processed and analyzed using spectral indices, SCA, MNF and PCA techniques using ENVI (5), ERDAS IMAGINE (2013), and Arc GIS (10.1) software packages. ASTER SWIR bands with spatial resolution 30 m were resampled using nearest neighbor resampling method to correspond to the VNIR 15-m spatial resolution. ASTER 6 SWIR and 3 VNIR bands were stacked to form 9 ASTER bands with 15-m spatial resolution data sets.

Minimum noise fraction transformation

MNF is used to determine the inherent dimensionality of the 9 ASTER data (VNIR and SWIR) to segregate and equalize the noise in the data and to reduce the computational requirements for subsequent processing (Green et al. 1988; Boardman and Kruse 1994). MNF has been applied on the 9 ASTER (SWIR and VNIR) bands.

Band ratio technique

This technique is useful for highlighting certain features or materials that cannot be emphasized in the individual raw band (Sabins 1999; Ninomiya 2003; Mars and Rowan 2006). Band ratio technique is applied on both Landsat 8 and ASTER data in

Table 4 Trace element contents (ppm) of Au, Ag, Cu, Pb, and Zn mineralization in alteration zones (types 1 and 2)

Alteration zone	Alteration zone type 1		Alteration zone type 2					
Elements	S 19	S 16	S 22	S 20	S 18	S 12	S 5	S 3
Au (ppm)	0.14	0.08	1.98	36.6	2.11	0.07	4.46	0.05
Ag (ppm)	N.D	N.D	0.7	200	0.3	3	1.9	0.6
Cu (ppm)	36.6	30.8	83,720	218.3	162.3	2,012	2,440	10,220
Pb (ppm)	32.5	21	6	6	17	16	33	6.4
Zn (ppm)	24.6	12.6	3,992	55.6	63	327	327	266

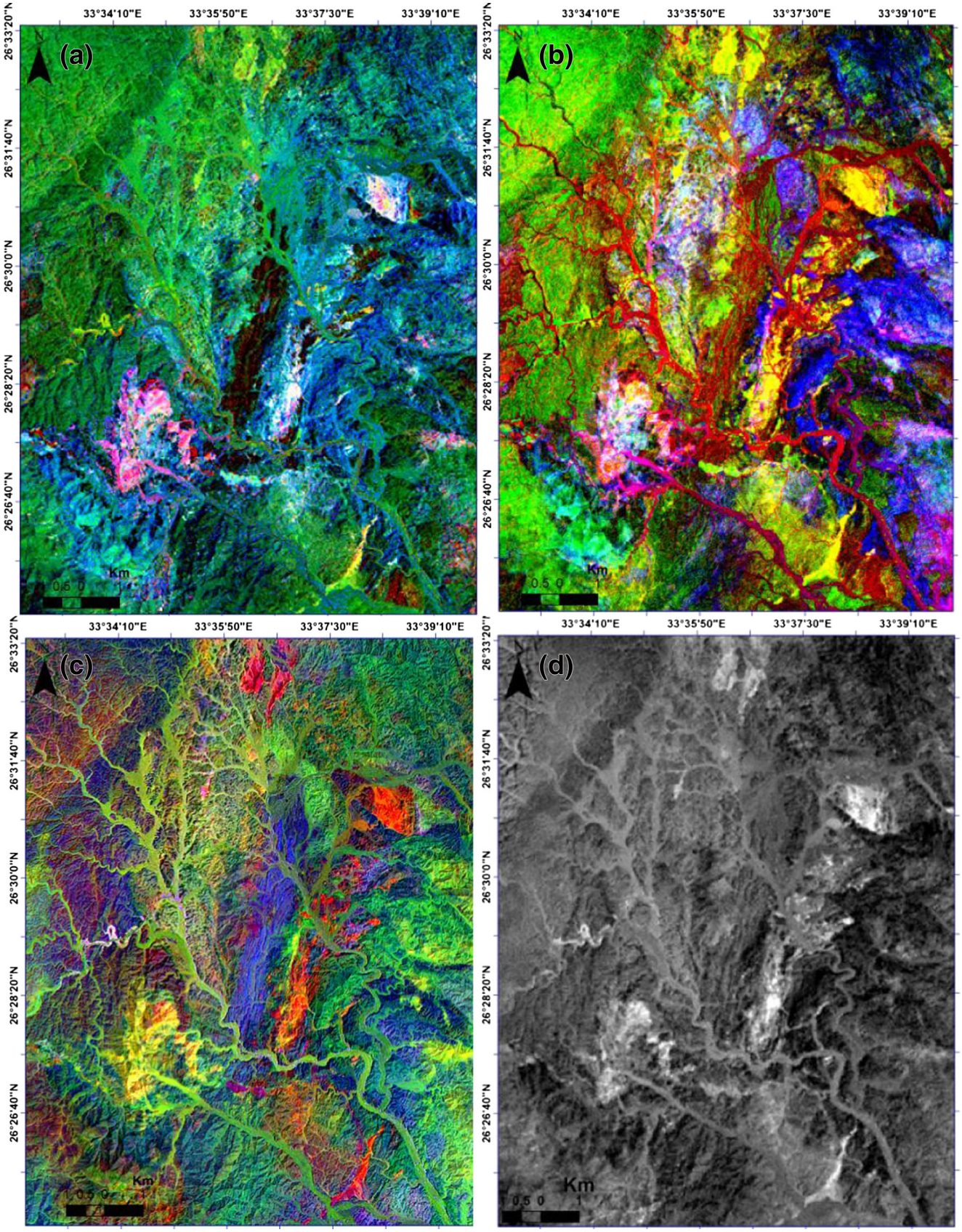

Fig. 5 **a** Landsat 8 band ratio image (b6/b2, b6/b7, b6/b5×b4/b5) on RGB. **b** ASTER MNF (2, 4, 8) on RGB image. **c** ASTER principal component image (PC4, PC3, PC6) on RGB. **d** ASTER band ratio (b4/b5) emphasizes the alteration zone with bright white tone at Abu Marawat-Semna and some other areas

order to enhance the discrimination of lithological units and the detection of alteration zones at the study area.

Principal component analysis

PCA is used to produce uncorrelated output bands by finding a new set of orthogonal axes that have their origin at the data mean and that are rotated so the data variance is maximized. The PCA technique (Pearson 1901) is a mathematical procedure used in image processing today that transforms a number of correlated spectral bands into a smaller number of uncorrelated spectral bands called principal components. Therefore, PCA enhances the separation of certain types of spectral signatures from the background. PCA was applied to the proposed ASTER band ratios to emphasize the distribution of the mineralized zone of the study area.

Field work

Some representative rock samples of the full range of lithologies of the area were collected as reference materials in mapping and classification of the different rock units of the study area. In addition, some samples from the alteration zones (Fig. 2) were also gathered for mineralogical and chemical investigations. The produced geological map of the area, using remote sensing techniques was revised and verified in the field whereas many field localities representing different lithological contacts and the alteration zones have been checked (see Fig. 10). The field investigations showed that the carbonates are the predominant constituents in the alteration zone related to the ophiolitic serpentinites at Semna area (Fig. 2a). On the other hand, the altered metavolcanics at Abu Marawat area are dissected by furriginated quartz veins (Fig. 2b). These rocks are silicified and kaolintized (Fig. 2c) and stained by malachite (Fig. 2d).

Laboratory work

X-ray diffraction (XRD) and XRF analyses have been carried out for the representative samples of the alteration zones. Au, Ag, Cr, Ni, Co, Cu, Pb, Zn, and Mo were analyzed using the Atomic Absorption technique (Model GBC-908). The analyses were carried out in the Central Laboratories of the Egyptian Mineral Resource Authority (EMRA).

Results and discussion

Mineralogical and chemical compositions of the alteration zones

Two alteration zones type 1 and type 2 with different compositions are recorded in the field in the Abu Marawat area. Only type 1 alteration zone is recorded at Semna area. The alteration zone type 1 is confined to the ultramafic ophiolitic rock units, while the alteration zone type 2 is found in more felsic rocks of the island-arc metavolcanics. The representative XRD data of both zones are given in Figs. 3 and 4 and Table 1. As seen in the given charts, the carbonates (magnesite, dolomite, and calcite) are predominant in type 1 alteration zone with the occurrence of minor quartz (Fig. 3). On the other hand, quartz, sericite, and kaolinite are the main mineralogical assemblage in type 2 alteration zone (Fig. 4) with minor alunite. However, the type 2 alteration zone at Abu Marawat area is characterized by the development of kaolinitization, silicification, and stained malachite (Fig. 2c, d). The type 1 alteration zone,

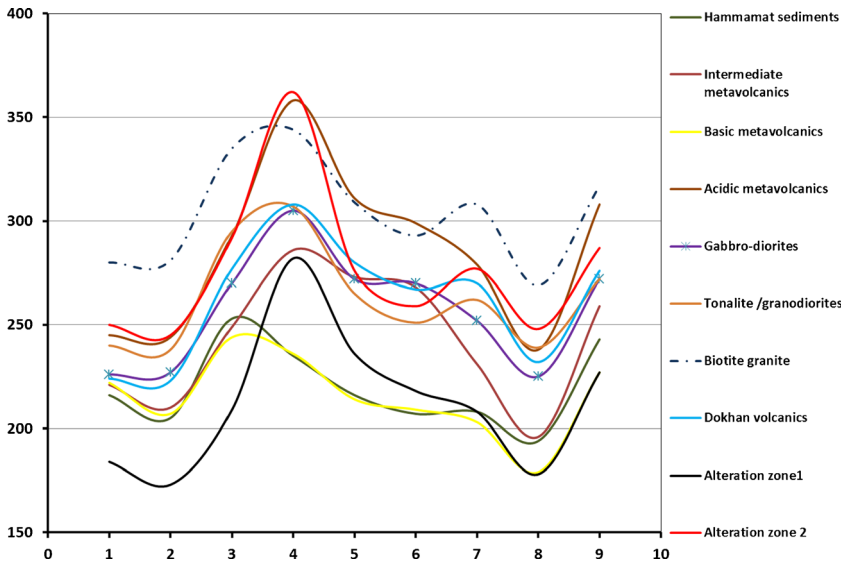

Fig. 6 Diagram showing the averaged DN value response in each of the ASTER VNIR_SWIR bands of the exposed rock units and alteration

which is confined to the serpentinite-talc-carbonate rock units, is characterized by the development of carbonatization. More detailed mineralogical and geochemical investigations initiated in this work is needed to evaluate the paragenetic sequences of these alteration types precisely to study their mutual relations and to trace potential listwaenite gold-bearing alteration zone.

Representative major chemical compositions of the alteration zone types 1 and 2 are given in Table 2. Obviously, the type 1 alteration zone as expected is characterized by low SiO_2 (16.5–12.2 wt%), Al_2O_3 (0.16–0.46 wt%), and K_2O content (up to 0.09 wt%), but by high abundances of MgO (22.5–18.1 wt%) and Fe_2O_3 (7.8 wt%) in accordance with their mineralogical data. By contrast, the alteration zone type 2 which is related to the more felsic metavolcanics is characteristically enriched in SiO_2 (75.56–74.05 wt%), Al_2O_3 (14.17–16.06 wt%), and K_2O content (up to 3.79 wt%), substantiating the XRD data.

The distribution of the trace elements of both alteration zones (Tables 3 and 4) mirror their major oxide compositions. The carbonatization zone (alteration type 1) is obviously

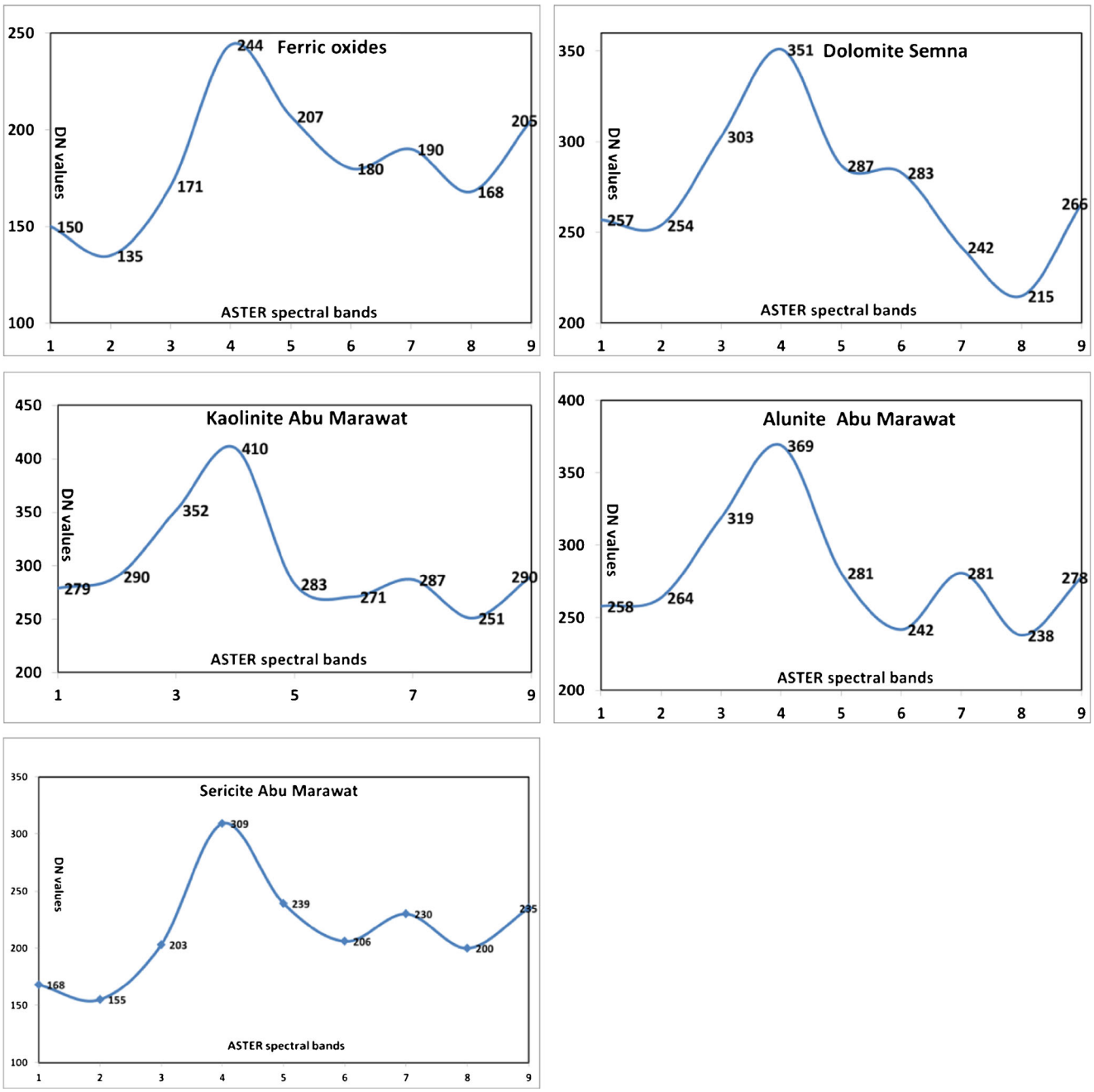

Fig. 7 Diagram showing the averaged spectral response in each of the ASTER VNIR-SWIR bands of the different mineralized zones in the study area

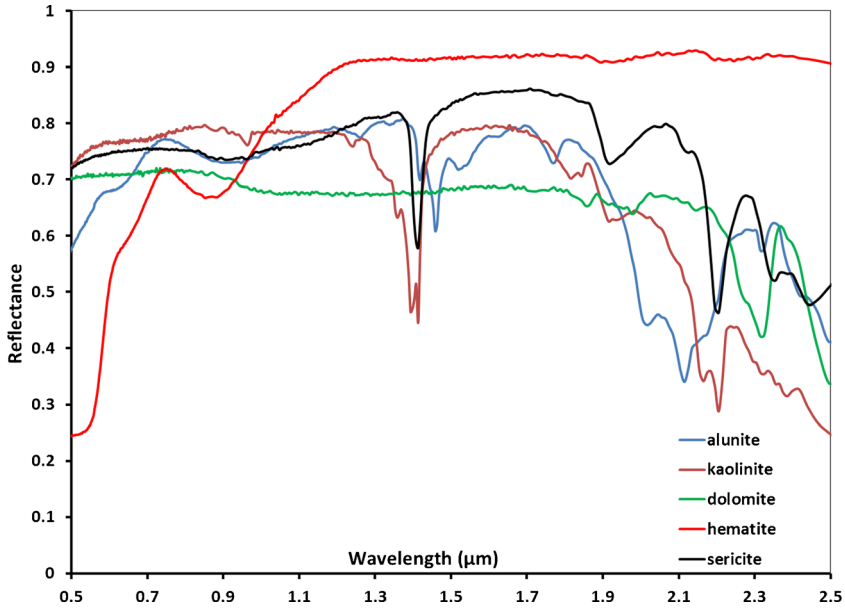

Fig. 8 Diagram showing the spectral response hematite within range from 0.5 to 2.5 μm of the alunite, kaolinite, dolomite, and ferric oxides (spectral library: usgs_min.sli available in Envi 5 software)

enriched in Cr (up to 1,549 ppm), Ni (up to 1,052 ppm), and Co (up to 70 ppm) indicating their derivation from ultramafic precursor (cf. Table 2). On the other hand, the type 2 alteration zone, which is confined to the more felsic island-arc metavolcanics is characterized by low contents of Cr (up to 33 ppm), Ni (~8 ppm), but high Ba (up to 524 ppm), consistent with their relatively higher K_2O (up to 3.79 wt%) content (cf. Tables 2 and 3). Of gold, silver, and some transition elements (Table 4), the type 2 alteration zone contains appreciable Au (36.6–0.05 ppm), Ag (up to 200 ppm), Pb (up to 33 ppm), Zn (up to 3,992 ppm), and Cu (up to 10,220 ppm) contents. The type 1 alteration zone (Table 4) exhibits Au content in the range of 0.14 to 0.08 ppm and low Cu content (up to 37 ppm). These data indicate that the alteration zones in the metavolcanics and the ophiolitic serpentinite-talc-carbonate rocks of the study area are prospective and need more detailed exploration for Au and Ag mineralization.

Lithological mapping

In general, each rock unit with its characteristic rock-forming minerals has its own reflectance signature. Hence, by using the remote sensing techniques, the different rock units in a particular area can be reasonably discriminated on the basis of their reflectance characteristics. As a result of alterations, new mineral phases might be formed at the expense of the primary phases or might be introduced to the system via hydrothermal activity. Such changes and differences between the mineral phases of particular altered and unaltered rock units may be discernible using remote sensing techniques. For example, Sabins (1999) monitored the enrichment of iron content in some altered rocks indicated by the higher red reflectance in the visible portion of the spectrum, compared to their fresh unaltered counterparts.

Generally speaking, the change in abundance of any mineral phase(s) in the alteration zones will likely lead to a minor change in the reflectance value and depending on that mineral's spectral characteristics compared to the relatively unaltered rock mass. In the study area, the spectral bands 2, 4, 5, 6, and 7 of Landsat 8 have been used in order to discriminate between the widely exposed rock units in the area under consideration, including altered and unaltered rocks. A new proposed band ratio image (6/2, 6/7, 6/5×4/5) of Landsat 8 (Fig. 5a) has been used for mapping and discriminating the acidic metavolcanics with yellowish green color, basic metavolanics with very dark green color, intermediate metavolcanics with blue color, and Hammamat sediments with very dark red color, while the serpentinite-talc-carbonate rocks are recognized as having bright red color at Semna and Abu Marawat areas. The results show that the alteration zones at Semna and Abu Marawat area are not discriminated in the proposed band ratio image (6/2, 6/7, 6/5×4/5) of Landsat 8 (Fig. 5a).

On the other hand, the geological interpretations of the extracted 9 ASTER MNF image show that the alteration zones with their associated lithological units can be better discriminated than with the previous proposed band ratio image (Fig. 5b). Two alteration zones in the MNF image (Fig. 5b)

Fig. 9 **a** ASTER Ferric oxides index (B4/B3). **b** ASTER dolomite index (B6+B8/B7). **c** ASTER Alunite index (B7/B5×B7/B8). **d** ASTER Kaolinite index (B4/B5×B8/B6). **e** ASTER sericite index (B5+B7/B6). **f** PC1, PC3, PC5 false color composite image on GRB ▶

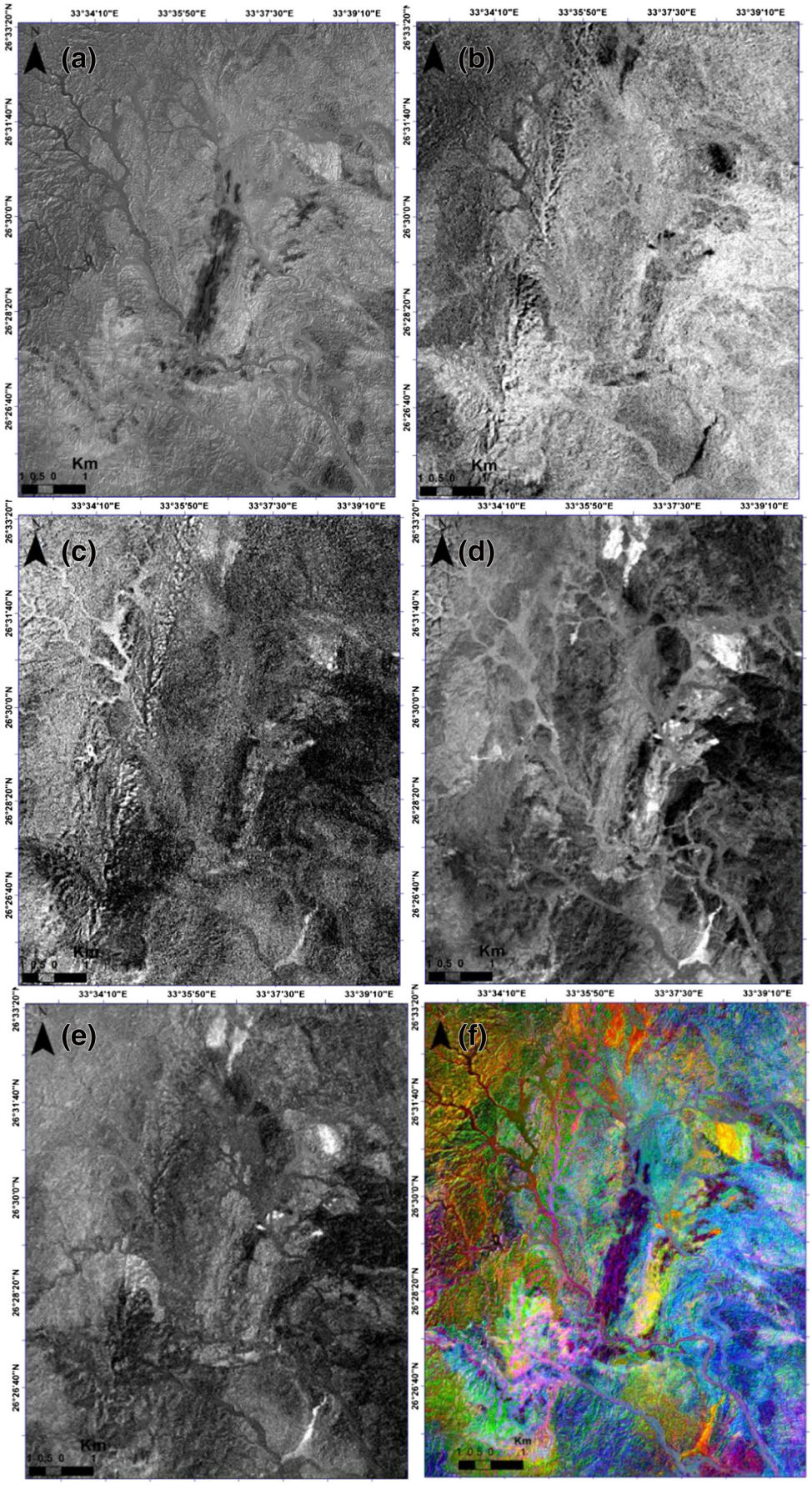
(a)
(b)
(c)
(d)
(e)
(f)
33°34'10"E
33°35'50"E
33°37'30"E
33°39'10"E
26°33'20"N
26°31'40"N
26°30'0"N
26°28'20"N
26°26'40"N
Km
1 0.5 0 1

are well-separated by pink and cyan colors in the Semna and by yellow color at Abu Marawat area.

PCA technique has been applied using 9 ASTER VNIR and SWIR bands. The resulting PCA image (PC4, PC3, PC6 on RGB) (Fig. 5c) was found to be sharper and easier to interpret than those images previously produced by the Landsat 8 band ratio and the ASTER MNF images. Acidic metavolcanics have light/reddish green colors, basic metavolcanics are yellowish green in color, metasediments have purple color, and intermediate metavolcanics have dark blue colors. Gabbro-diorite has greenish purple color and is not easily distinguished. Tonalite/granodiorite has dark purple to blue color. The biotite granite has brownish purple color. Using the visual interpretation, the two alteration zones in the PC4, PC3, PC6 (Fig. 5c) image are well-separated by orange color at Semna and by yellow color at Abu Marawat.

Detection of alteration zones

Alteration zones are controlled by type of host rock, nature of the mineralizing fluid, and style of deformation of host rocks (Rose and Burt 1979). As previously stated, the mineralogical compositions of the alteration zones types 1 and 2 involve magnesite, dolomite, calcite, quartz, sericite, kaolinite, and alunite in addition to iron oxides and pyrite. The effect of hydrothermal solutions on the feldspar crystal lattice has resulted in the liberation of Fe^{2+} that is then oxidized and precipitated as haematite micro-inclusions, conferring the red and reddish-brown colors to the altered minerals.

The band ratio (b4/b5) has been applied to separate the altered mineralized zones (Fig. 5d). The iron oxide-rich parts of the alteration zone are considered the main target for gold exploration, and due to the spectral and spatial capabilities of the ASTER images, the collected spectral information about well-known targets are used to identify the potential mineralized areas in the alteration zones. For this purpose, ASTER VNIR & SWIR surface reflectance data have been used to obtain spectral information about target areas that were discriminated in the field as altered mineralized rocks as well as the surrounding exposed rock units (Fig. 5). The spectral measurements were taken over and around the old workings sites of the Abu Marawat and Semna areas and the calculated average spectra are plotted in (Fig. 6).

The average spectral curves for some mineralized rocks (Fig. 7) show more or less a general agreement, with some exceptions, compared to the USGS ASTER spectral library (Fig. 8). The average spectra for the altered mineralized rocks show the same lower reflectance in ASTER bands 2, 6, and 8 compared to the ASTER band 4 and 7 (equivalent to bands 6 and 7 in Landsat 8 data), while in the visible portion of the spectrum only the ASTER band 1 (equivalent to band 3 in Landsat 8) of the altered mineralized rocks has a high spectral reflectance (Fig. 7). The USGS spectral library of rock-forming minerals (available in Envi 5 software, spectral library: usgs_min.sli), was used to identify the five alteration minerals (alunite, kaolinite, dolomite, sericite, and ferric oxides) from the reflectance 0.5 to 2.5 μm data (Fig. 8).

Accordingly, ASTER band ratio (b4/b3) discriminate the iron ores (Fig. 9a) because magnetite (ferric iron) has strong spectral absorption features around 0.88 and 0.52 μm. For the other alteration phases and according to Ninomiya (2003), ASTER (6+8/7) (Fig. 9b) is applied for dolomite index which has absorption features at 1.8 and 2.32, while the ASTER band ratio (b7/b5×b7/b8) (Fig. 9c) is used for alunite index which has absorption features at 1.42, 1.76, 2.16, and 2.4 μm. On the other hand, the ASTER band ratio (b4/b5×b8/b6) (Fig. 9d) has been applied to characterize kaolinite index which has absorption features at 1.42 and 2.2 μm and ASTER band ratio (5+7/6) (Fig. 9e) has been applied for sericite index which has absorption features at 1.42 and 2.21.

Hence, from the derivative gray-scale images (Fig. 9a–e), the concentrations of the different alteration phases (alunite, kaolinite, ferric oxides, sericite, and dolomite) in the study area were evaluated using VNIR and SWIR as follows: (a) ferric oxide index shows more or less the same concentration at both Abu Marawat and Seman areas (Fig. 9a), (b) dolomite and alunite indices (b and c of Fig. 9, respectively) show high concentration at Abu Marawat area, (c) kaolinite and sericite

Table 5 Eigenvector loadings and Eigenvalues of PCs for the derivatives spectral indices (highlighted yellow cells represent the highest Eigenvector loadings)

Mineral index	PC1	PC2	PC3	PC4	PC5	PC6
B4/B5 (alteration zones)	0.003999	0.000255	−0.55942	−0.17747	−0.20196	−0.78406
B4/B3 (Ferric oxides)	0.003787	0.002352	0.129261	−0.97889	0.124921	0.097184
B5+B7/B6 (Sericite)	0.7309	−0.68243	0.007308	0.002163	0.002242	−0.00278
B6+B8/B7 (Dolomite)	0.682442	0.730921	0.000198	0.004765	0.000926	0.00226
B4/B5×B8/B6 (Kaolinite)	0.003722	−0.00514	−0.79294	−0.00841	0.391357	0.466873
B7/B5×B7/B8 (Alunite)	0.003816	−0.00295	−0.20378	−0.10092	−0.88907	0.397272
Eigenvalues	71.88505	5.891007	0.016048	0.012686	0.000673	0.0000236
Information%	92.39072	7.571454	0.020626	0.016305	0.000865	0.000030

indices (d and e of Fig. 9, respectively) show higher concentration at Abu Marawat with some new occurrences southward, compared to Semna area. Thus, this approach may be of service in producing preliminary exploration maps for detecting and evaluating such characteristic alteration phases in other potentially gold-bearing areas in arid regions.

Some authors (e.g., Zhang et al. 2007; Gabr et al. 2010) employed the PCA combined with other band ratios to enhance mineral information. In the present study, we apply the PCA combined with the derivative ASTER band ratios which emphasize the distribution of the minerals of the two alteration zones (Semna and Abu Marawat). The extracted PCA eigenvector loadings and eigenvalues (Table 5) show the following: (a) PC1 image correlates with sericite which show positive eigenvector values (0.73), (b) PC2 image correlates with dolomite image which show high positive eigenvector values (0.73), (c) PC3 and PC4 show high negative eigenvector values for kaolinite (−0.79) and ferric oxides (−0.97) respectively, (d) PC5 has high negative eigenvector loadings for alunite (−0.88) while PC6 has high negative eigenvector loadings (−0.78) for the detected alteration zones type 1 and type 2.

The alteration zones and their related minerals were mapped using PC1, PC3, and PC5 on GBR image of mineralogical indices (Fig. 9f). This image shows the kaolinite with orange color, sericite with green color and alunite with yellow color. The field data with the results of interpretation of the different ASTER derivatives (band ratio and MNF) images were used to produce a detailed geological map of the study area with the detection and discrimination of the alteration zones (Fig. 10). The present new map which was verified in the field contributes significantly to the previously published

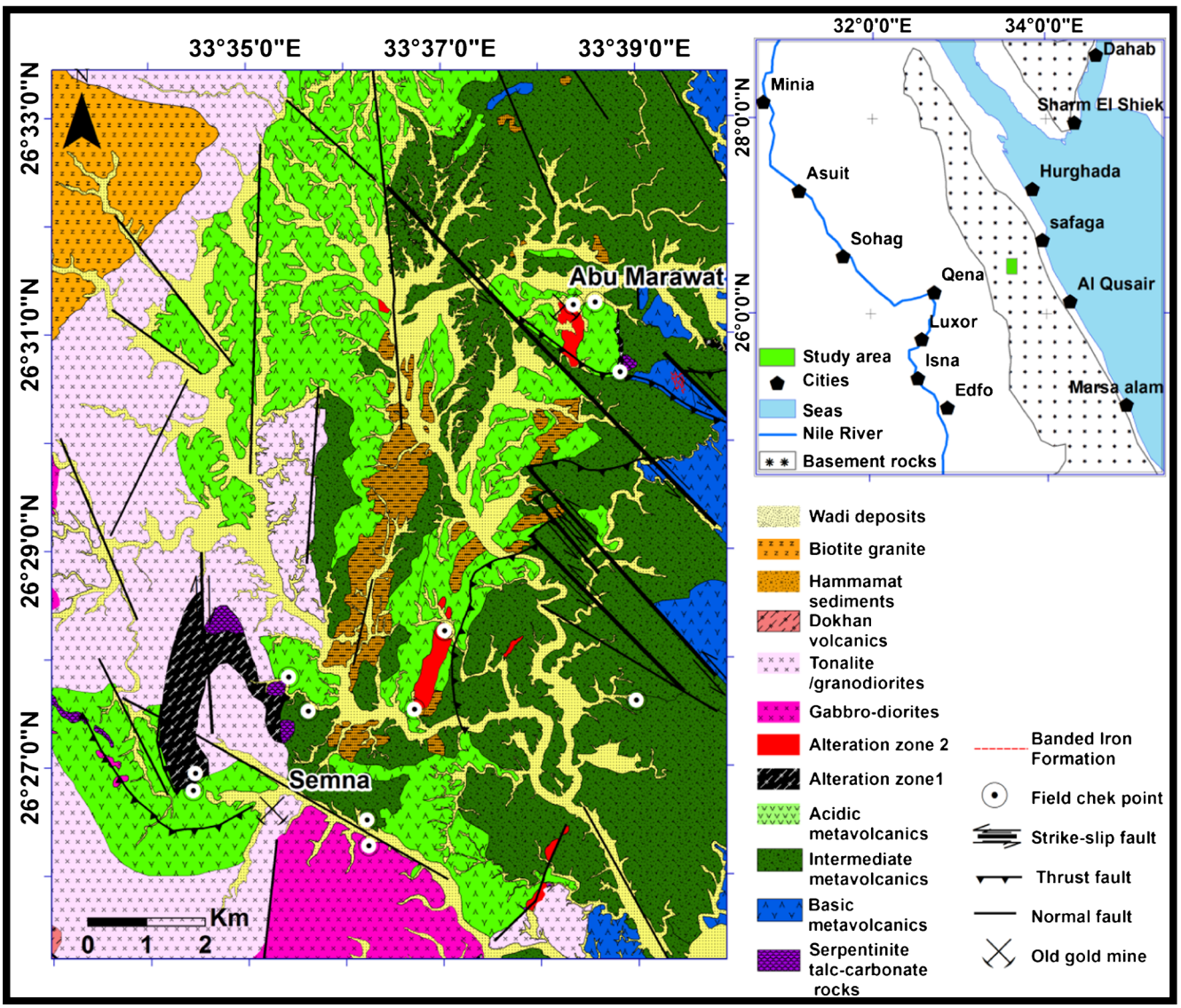

Fig. 10 **a** Detailed geological map of the study area using the integrated data of Landsat 8 band ratio, ASTER PCA, and ASTER MNF images. b Location map of the study area

geological maps (EGSMA 1992; Gabr et al. 2010 and Zoheir et. al. 2008) of the area in terms of the distribution of some rock units and their mutual contacts. The most prominent advantage of the proposed geological map (Fig. 10) is the discrimination of the alteration zones at Abu Marawat (alteration zone type 2) and Semna (alteration zone type 1) for the first time, as well as modification of some lithological contacts.

Conclusions

This study explores performance characteristics of ASTER as a tool for mapping the basement rock units of Abu Marawat-Semna area and their hydrothermal mineralized alteration zones (alteration zones 1 and 2). The area is occupied by ophiolitic, island-arc assemblages (metavolanics and gabbro-diorite) in addition to the younger granitoids. In mapping, four types of algorithms have been used to extract spectral information of ASTER VNIR and SWIR reflectance product: (1) spectral characteristic analysis, (2) band ratio; (3) principal components and enhancement-based methods such as PCA; and (4) MNF. It has been found that ASTER data can be best processed and analyzed to obtain information about the spatial distribution of the hydrothermal gold-bearing alteration zones at the Abu Marawat-Semna area. These alteration zones have been verified by field investigation as well as mineralogical and geochemical studies.

Remote sensing, field study, and laboratory investigations revealed that there are two types of alteration zones in the study area. The type 1 alteration zone occurs in ultramafic rocks of ophiolitic origin at Abu Marawat and Semna areas and is characterized by carbonatization and evolution of magnesite, dolomite, and calcite as the main phases. On the other hand, the type 2 alteration zone occurs at Wadi Abu Marawat and is characterized by kaolanization, silicification, and staining by malachite. It consists essentially of sericite, kaolinite, alunite, and quartz and it is associated with sulfides and is promising for hosting and concentrating gold content.

The geochemical studies recorded anomalous contents of chromite, nickel, and cobalt in the type 1 alteration zone, whereas the Cr reaches up to 1,549 ppm, Ni abundance attains about 1,052 ppm, and Co reaches about 70 ppm. The investigated type 2 alteration zone in the metavolcanic rocks recorded the presence of high anomalous contents of gold (up to 36 ppm), silver (up to 200 ppm), zinc (up to 3,992 ppm), and copper (up to 83,720 ppm). The geochemical study indicates that the alteration zones in the metavolcanics and the ophiolitic serpentinite-talc-carbonate rocks are promising and need more detailed exploration for Au and Ag mineralization. The study proved the potentiality of the alteration zones in and around these ophiolitic ultramafic rocks and their intimately surrounding island-arc metavolcanics in the Egyptian basement sequences for further gold exploration. Image processing of the remote sensing data as proposed in the present study proves its high capability in detecting the mineralized alteration zones in other tectonically and geologically similar arid regions in the Arabian-Nubian Shield (ANS) and worldwide.

Acknowledgments The authors would like to express their thanks to the staff members in the National Authority for Remote Sensing and Space Sciences (NARSS) for their valuable discussions and great help and for providing the ASTER data. Authors are very thankful to the reviewers for their valuable reviews and suggestions and to the editor of the journal for careful editing of the paper that has helped to present the work clearly.

References

Abdelsalam MG, Stern R (2000) Mapping gossans in arid regions with landsat TM and SIR-C images, the Beddaho Alteration Zone in northern Eritrea. J Afr Earth Sci 30(4):903–916

Abou Elmagd K, Emam A, Ali-Bik MW (2013) Chemostratigraphy, petrography and remote sensing characterization of the Middle Miocene - Holocene sediments of Ras Banas peninsula, Red Sea Coast. Egypt Carpathian J Earth Environ Sci 8(3):27–42

Abrams MJ, Hook SJ (1995) Simulated ASTER data for geologic studies. IEEE Trans Geosci Remote Sens 33:692–699

Ali-Bik MW, Taman Z, El Kalioubi B, Abdel Wahab W (2012) Serpentinite-hosted talc-magnesite deposits of Wadi Barramiya area, Eastern Desert, Egypt: characteristics, petrogenesis and evolution. J Afr Earth Sci 64:77–89

Aly NA, Hegazy HA, El-Tigrawy AA (1991) Geology and petrochemistry of the arc volcanics in the Semna area, southwest of Safaga. Egypt Bull Fac Sci Assuit Univ 20:61–78

Amer R, Kusky T, El Mezayen A (2012) Remote sensing detection of gold related alteration zones in Um Rus area, Central Eastern Desert of Egypt. Adv Space Res 49:121–134

Amer R, Kusky T, Ghulam A (2010) Lithological mapping in the Central Eastern Desert of Egypt using ASTER data. J Afr Earth Sci 56:75–82

Basta FF, Takla MA, Maurice AE (2000) The Abu Marawat banded iron formation: geology, mineralogy, geochemistry and origin. 5th International Conference on the Geology of the Arab World, Cairo University, ARE, 319-334

Bishara WW, Habib ME (1973) The Precambrian banded iron ore of Semna, Eastern Desert. Egypt N Jb Miner Abh 120(1):108–118

Boardman JW, Kruse FA (1994) Automated spectral analysis: a geological example using AVIRIS data, north Grapevine Mountains, Nevada: in Proceedings, ERIM Tenth Thematic Conference on Geologic Remote Sensing, Environmental Research Institute of Michigan, Ann Arbor, MI, I-407 - I-418

Botros NS (1991) Geological and geochemical studies on some gold occurrences in the north Eastern Desert, Egypt. Unpublished Ph.D. Thesis, Zagazig University, p 146

Botros NS (1993b) New prospects for gold mineralization in Egypt. Ann Geol Surv Egypt 19:47–56

Botros NS (1995a) Genesis of gold mineralization in the North Eastern Desert, Egypt. Ann Geol Surv Egypt 20:381–409

Botros NS (1995b). Stratiform gold deposits in a Proterozoic BIF, Abu Marawat area, Eastern Desert, Egypt. Abstract, 11th Symposium on Precambrian and Development, Cairo, Egypt

Botros NS (2002a) Metallogeny of gold in relation to the evolution of the Nubian Shield in Egypt. Ore Geol Rev 19:137–164

Botros NS (2002b) Alteration zones: are they good target for gold deposits in Egypt. Arab Gulf J Sci Res 20:209–218

Botros NS (2004) A new classification of the gold deposits of Egypt. Ore Geol Rev 25:1–37

Chang C-I, Heinz DC (2000) Constrained subpixel target detection for remotely sensed imagery. IEEE Trans Geosci Remote Sens 38: 1144–1159

Crósta AP, Filho CRS (2003) Searching for gold with ASTER. Earth Obs Mag 12(5):38–41

Cudahy TJ, Okada K, Yamato Y, Huntington JF, Hackwell JA (2000) Mapping skarn alteration mineralogy at Yerington, Nevada, using airborne hyperspectral TIR SEBASS imaging data. ERIM Proceedings of the 14th International Conference on Applied Geologic Remote Sensing, 70–79

Dardir AA, Al-Wakeel MI (1998) Geology, petrology and radioactivity of Gabal Um Tagher Gabal Abu Furud area, Central Eastern Desert. Egypt Egyp J Geol 42:75–103

David JH (1988) Abu Marawat prospect, Central Eastern Desert of Egypt. A Review an Assessment of Work Carried Out by Minex-Minerals, Egypt. Internal report, Geolog Surv Egypt

Di Tommaso I, Rubinstein N (2007) Hydrothermal altration mapping using ASTER data in the Infiernillo porphyry deposit, Argentina. Ore Geol Rev 32:275–290

EGSMA (1992) geologic map of Al QUSAYR QUADRANGLE, EGYPT. SCALE, 1:250000

El Gaby S, List FK, Tehrani R (1988) Geology, evolution and metallogenesis of the Pan-African Belt in Egypt, in: El Gaby, S., Greiling, R. (Eds.), The Pan-African Belt of NE Africa and adjacent areas, Tectonic Evolution and Economic Aspects. Freidr Vieweg and Sohn, Braunschweig/Weisbaden, p. 17–68

El Gaby S, List FK, Tehrani R (1990) The basement complex of the Eastern Desert and Sinai. In: Said R (ed) The Geology of Egypt. A. A. Balkema, Rotterdam, pp 175–184

El-Shazly SM, El-Sayed MM (2000) Petrogenesis of the Pan-African El-Bula igneous suite, Central Eastern Desert. Egypt J Earth Sci 31: 317–336

El-Mezayen AM, Hassaan MM, El-Hadad M, Hassanein MM (1995) Petrography, geochemistry and ore microscopy of Abu Marawat metavolcanics and associated gold mineralization, North Eastern Desert, Egypt. Bulletin of Faculty of Science, Al-Azhar University, 6 (2), 1999-2021

Farahat E, Mohamed H, Ahmed A, El-Mahallawi M (2007) Origin of I- and A-type granitoids from the Eastern Desert of Egypt: implications for crustal growth in the northern Arabian–Nubian Shield. J Afr Earth Sci 49:43–58

Fowler A, Ali KG, Omar SM, Eliwa HA (2006) The significance of gneissic rocks and synmagmatic extensional ductile shear zones of the Barud area for the tectonics of the North Eastern Desert. Egypt J Afri Earth Sci 46:201–220

Ferrier G, White K, Griffiths G, Bryant R (2002) The mapping of hydrothermal alteration zones on the island of Lesvos, Greece using an integrated remote sensing dataset. Intern J Remote Sens 23(2): 341–356

Fujisada H (1995) Design and performance of ASTER instrument: Proceedings of the International Society for Optical Engineering, v. 2583, p 16–25

Fujisada H (1995) Design and performance of ASTER instrument: Proceedings of the International Society for Optical Engineering 2583: 16–25

Gabr S, Ghulam A, Kusky T (2010) Detecting areas of high-potential gold mineralization using ASTER data. Ore Geol Rev 38:59–69

Gad S, Kusky TM (2007) ASTER spectral ratioing for lithological mapping in the Arabian-Nubian shield, the Neoproterozoic Wadi Kid area, Sinai, Egypt. Gondwana Res 11(3):326–335

Green AA, Berman M, Switzer P, Craig MD (1988) A transformation for ordering multispectral data in terms of image quality with implications for noise removal. IEEE Trans Geosci Remote Sens 26(1):65–74

Hassan MA, Hashad AH (1990) Precambrian of Egypt. In: Said R (ed) The geology of Egypt. Balkema, Brookfield, pp 201–245

Hume ME (1937) Geology of Egypt, Volume II, Part II. Geological Survey of Egypt. Kennedy W.Q., 1964. The structural differentiation of Africa in the Pan-African (±500 m.y.) tectonic episode. 8th Annual Report of the Research Institute of African Geology. University of Leeds, U.K., 48–49

Kröner A (1984) Late Precambrian plate tectonics and orogeny: a need to redefine the term Pa African. In: Klerkx J, Michot J (eds) Geologie Africaine, African Geology. Musee Royal de l'Afrique Centrale, Tervuren, pp 23–28

Kröner A, Muhongo S, Sommer H, Vogt M (2003) The East African Orogen: accretion versus collision. European Geophysical Society, Geophysical Research Abstracts 5 (#6608), 6–11

Kusky TM, Ramadan TM (2002) Structural controls on Neoproterozoic mineralization in the South Eastern Desert, Egypt: an integrated field, Landsat TM and SIR-C/X SAR approach. J Afri Earth Sci 35:107–121

Kusky TM, Abdelsalam MG, Tucker RD, Stern RJ (2003) Evolution of the East African and related orogens, and the assembly of Gondwana. Precambrian Res 123:81–85

Liu F, Wu X, Sun H, Guo Y (2007) Alteration Information Extraction by Applying Synthesis Processing Techniques to Landsat ETM+Data: Case Study of Zhaoyuan Gold Mines, Shandong Province, China. J China Univ Geosci 18(1):72–76

Loughlin WP (1991) Principal components analysis for alteration mapping. Photogramm Eng Remote Sens 57:1163–1169

Mars JC, Rowan LC (2006) Regional mapping of phyllic-and argillic-altered rocks in the Zagros magmatic arc, Iran, using Advanced Spaceborne Thermal Emission and Reflection Radiometer (ASTER) data and logical operator algorithms. Geosphere 2(3): 161–186

Mohamed FH, El-Sayed MM (2007) Post-orogenic and anorogenic A-type fluoritebearing granitoids, Eastern Desert, Egypt: petrogenetic and geotectonic implications. Chemie der Erde-Geochem 68:431–450

Ninomiya YA (2003) Stabilized vegetation index and several mineralogic indices defined for ASTER VNIR and SWIR data, in: Proceedings of IEEE. Inter Geosci and Remote Sens Symp (IGARSS) 3:1552–1554

Pearson K (1901) On lines and planes of closest fit to systems of points in space. Philos Mag 2:559–572

Rajendran S, Nasir S, Kusky TM, Ghulam A, Gabr S, El-Ghali AKM (2013) Detection of hydrothermal mineralized zones associated with listwaenites in Central Oman using ASTER data. Ore Geol Rev 53: 470–488

Ramadan TM, Abdelsalam MG, Stern RJ (2001) Mapping gold-bearing massive sulfide deposits in the Neoproterozoic Allaqi suture, SE Egypt with Landsat TM and SIRC/ X-SAR images. J Photogramm Eng Remote Sens 67(4):491–497

Rokos D, Argialas D, Mavrantza R, St.-Seymour K, Vamvoukakis C, Kouli M, Lamera S, Paraskevas H, Karfakis I, Denes G (2000) Structural mapping and analysis for a preliminary investigation of possible gold mineralization by using remote sensing and geochemical techniques in a GIS environment: study area: island of Lesvos, Aegean Sea, Hellas. Nat Resour Res 9:277–293

Rose AW, Burt DM (1979) Hydrpthermal Altration, Chapter, 5, Geochemistry of Hydrothermal Ore Deposits, 2nd Ed

Rowan LC, Mars JC (2003) Lithologic mapping in the Mountain Pass, California area using Advanced Spaceborne Thermal Emission and Reflection Radiometer (ASTER) data. Remote Sens Environ 84(3): 350–366

Rowan LC, Hook SJ, Abrams MJ, Mars JC (2003) Mapping hydrothermally altered rocks at Cuprite, Nevada, using the Advanced Spaceborne Thermal Emission and Reflection Radiometer (ASTER). A new satellite-imaging system. Econ Geol 98(5):1019–1027

Sabet AH, Tsogoev VB, Bordonosov VP, Babourin LM, Zalata AA, Francis MH (1976) On gold mineralization in the Eastern Desert of Egypt. Ann Geol Surv Egypt 6:201–212

Sabet AH, Bordonosov VP (1999) The gold ore formations in the Eastern Desert of Egypt. Annals Geological Survey of Egypt 16, 35-42, 1984. Sabins, F.F. Remote sensing for mineral exploration. Ore Geol Rev 14:157–183

Sabins FF (1997) Remote sensing principles and interpretation. W. H. Freeman Company, New York, pp 366–371

Sabins FF (1999) Remote sensing stratigies for mineral exploration. In: Rencz A (ed) Remote sensing for the earth sciences-manual of remote sensing. American Society of Photogrammetry and Remote Sensing/John Wiley and Sons, New York, pp 375–447

Sadek MF (2004) Discrimination of basement rocks and alteration zones in Shalatein area, Southeastern Egypt using Landsat Imagery data. Egypt J Remote Sens Space Sci 7:89–98

Sadek MF (2005) Geology and spectral characterization of the basement rocks at Gabal Gerf area Southeastern Egypt. Egypt J Remote Sens Space Sci 8:109–128

Sadek MF, Hassan SM (2012) Application of Egyptsat-1 and Landsat-ETM data fusion in discrimination of volcanic and granitic rocks at Gabal Gharib area, northeastern Egypt. Austr J of Basic Appl Sci 6(13):471–480

Settle J (2002) On constrained energy minimization and the partial unmixing of multispectral images. IEEE Trans Geosci Remote Sens 40:718–721

Stern RJ (1994) Arc assembly and continental collision in the Neoproterozoic East African Orogen: implications for the consolidation of Gondwanaland. Ann Rev Earth Plan Sci 22:319–351

Sultan M, Arvidson RE (1986) Mapping of serpentinites in the Eastern Desert of Egypt by using Landsat Thematic Mapper data. J Geol 14(12):995–999

Xu Y, Lin Q, Shao Y, Wang L (2004) Extraction mechanism of alteration zones using ASTER imagery. Geoscience and Remote Sensing Symposium, IGARSS'. Proceedings. IEEE Int 6:4174–4175

Zhang X, Pazner M, Duke N (2007) Lithological and mineral information extraction for gold exploration using ASTER data in the south Chocolate Mountains, California. ISPRS J Photogramm Remote Sens 62:271–282

Zoheir B, Akawy A, Hassan I (2008) Role of fluid and wallrock sulfidation in gold mineralization at Semna mine area, Central Eastern Desert of Egypt: Evidence from hydrothermal altration, fluid inclusions and stable isotope data. Ore Geology Reviews, 34(4):580–596

Zoheir B, Emam A (2012) Integrating geologic and satellite imagery data for high-resolution mapping and gold exploration targets in the South Eastern Desert. Egypt J Afri Earth Sci 66-67:22–34